sustainability

MDPI

Article

CFD-Based J-Shaped Blade Design Improvement for Vertical Axis Wind Turbines

Antonio García Auyanet, Rangga E. Santoso, Hrishikesh Mohan, Sanvay S. Rathore, Debapriya Chakraborty and Patrick G. Verdin *

Energy & Sustainability, Cranfield University, Cranfield MK43 0AL, UK
* Correspondence: p.verdin@cranfield.ac.uk

Abstract: The need for an increase in energy harvesting has led to novel ideas and designs to extract more power from wind. One innovative solution is through the use of J-shaped blades for Darrieus vertical axis wind turbines (VAWTs), which is based on the removal of a portion of a conventional blade, either on the pressure or suction side. Although improvements in the self-starting capabilities of VAWTs have been reported when using such blades, the literature only studied hollow blades, showing a hair-like structure. This work numerically investigates six different J-shaped designs. A turbine comprising NACA0015-based blades forms the base case and is used to evaluate the 2D numerical models. Results show that blades with an external cut systematically outperform those designed with an internal cut. In addition, all proposed cut-based designs are shown to improve the starting torque of the turbine, reaching a 135% increase compared to the base model.

Keywords: blade optimization; VAWT; starting torque; J-shape; NACA0015; CFD; k-ω

check for updates

Citation: García Auyanet, A.; Santoso, R.E.; Mohan, H.; Rathore, S.S.; Chakraborty, D.; Verdin P.G. CFD-Based J-Shaped Blade Design Improvement for Vertical Axis Wind Turbines. *Sustainability* **2022**, *14*, 15343. https://doi.org/10.3390/su142215343

Academic Editors: Higinio Sánchez-Sáinz and Raúl Sarrias-Mena

Received: 20 October 2022
Accepted: 15 November 2022
Published: 18 November 2022

Publisher's Note: MDPI stays neutral with regard to jurisdictional claims in published maps and institutional affiliations.

Copyright: © 2022 by the authors. Licensee MDPI, Basel, Switzerland. This article is an open access article distributed under the terms and conditions of the Creative Commons Attribution (CC BY) license (https://creativecommons.org/licenses/by/4.0/).

1. Introduction

The idea of building sustainable energy systems has gained popularity in the past decade due to the depletion of fossil fuels, increased demands for energy, climate change, and global warming. From the various available sustainable sources of energy, wind has proven to be quite valuable [1]. Over the years, the design and purpose of wind turbines have changed in order to become a potential source for powering homes across the world [2].

Turbines are classified as Horizontal Axis Wind Turbines (HAWT) and Vertical Axis Wind Turbines (VAWT) based on their axis of rotation. VAWTs are further divided into 3 sub-classes: the Savonius-type which is drag-based, the Darrieus-type, and the H-types, which are lift-based [2]. Compared to HAWTs, these types of turbines are less efficient, especially the Darrieus-type, due to their low torque output in the starting stages, which makes them rather unpopular. In addition, Darrieus turbines are characterized by unstable flow conditions inside their rotor. This is caused by the periodic changes of the local angle of attack experienced by the blades as they rotate, leading to vortex formation and shedding [3].

Numerous studies have been carried out in recent decades, aiming toward improving the efficiency of both HAWTs and VAWTs. Part of the effort has focused on small-scale devices for urban areas, for which low wind-speed has a large impact on the turbine's performance. Diffuser-augmented wind turbines (DAWT) for HAWTs have thus been the object of recent investigations [4,5]. For such devices, the rotor is surrounded by a duct, to increase the mass of air inside the turbine, and, thus, the power output [6]. Recent studies on DAWT have covered the analysis of ducts with several design variations, including the addition of a brim [7] or a flap [8].

As part of the research on VAWTs, several investigations have considered symmetric blades, based on airfoils such as NACA0012, NACA0015, and NACA0018. However, those

blades were unable to self-start the turbine and required a small amount of starting torque. Studies have shown that the use of a NACA 6-digit airfoil improved the performance of the curved blades of a VAWT [9]. Others suggested the use of a cambered airfoil to offer some additional design advantages and improve the power coefficient [10,11]. Experiments also showed that a modified NACA0018 airfoil could improve performance under no-load conditions [12]. Elsewhere, a modified NACA0018 was considered, and a new special-purpose airfoil named DU 06-W-200 was designed by changing the thickness and camber of the original airfoil [13]. In addition, studies for instance from [14], showed an improvement in the power coefficient for a model combining Savonius and Darrieus blade geometries.

Due to their self-starting issues, VAWTs require a mechanism to start functioning at low tip speed ratios (TSR, also denoted λ), either through a mechanical/electrical procedure or through changes in the original design. The previous paragraph described several studies that aimed to improve the starting capabilities by changing the airfoil profile. However, other design strategies have been investigated, such as the use of helical blades, or the addition of flaps or vortex generators to the blades [15], and the use of augmentation technologies on vertical DAWT [4,16]. Slotted blades have also been investigated recently [17,18]. One innovative idea was through opening the blade trailing edge, and forming what is called a J-shaped blade [19,20]. The geometry of a J-shaped airfoil is similar to a conventional airfoil on one side, and consists of a notch on the other side, with the location of the notch (inwards or outwards) dependent on the design considered. Such a design seems to provide a higher starting torque of the wind turbine due to the 'cup' shape, typical of Savonius-type blades, and a better overall efficiency due to the Darrieus-type blades after self-starting.

Numerical studies on J-shaped airfoils [19,20] have demonstrated that the self-starting ability of a VAWTs could be improved using an opening on the airfoil. Research indeed showed an almost linear starting torque enhancement with a cut in the outer part of the blade [19]. However, a decrease in the turbine performance also appeared in normal working conditions and the authors reported internal cut ratios between 0.48 and 0.6, and external cut ratios between 0.72 and 0.84 as favourable options for their turbine [19]. Other studies by Zamani et al. [20,21] showed an increase in turbine performance in normal working conditions, in addition to a starting torque enhancement. They conducted 2D studies of a turbine with DU 06-W-200 airfoils [20], and 3D studies of a turbine with NACA0015-based blades [21], and compared the results with the corresponding J-shaped based turbines (J-shapes created from DU 06-W-200 airfoils for the 2D case, and J-shapes created from NACA0015-based blades for the 3D case). Negative torque values were obtained during the rotation of the 3D NACA-based blades, which were explained by stall effects [21]. However, the J-shaped airfoils produced overall greater torque with no negative values. Hence the fatigue stress and vibrations on the blades were also reduced until the optimum TSR value, $\lambda = 1.6$.

Other authors had different views, they claimed that a J-shaped blade design does not provide any performance enhancement [22], and they did not recommend their use for Darrieus-type VAWTs. It should be noted, however, that the study reported in [22] was focused on turbines with solidity values between 0.1 and 0.2 and operating in the high TSR region. Those operating conditions are different from the ones used in the original papers [20,21] on J-shaped turbines.

Based on the conclusions from [22], further research was performed here to evaluate the effect of the solidity and λ on the performance of Darrieus VAWTs. Two main regions are usually considered for the operational regions of Darrieus turbines, either operating in the high TSR region (λ = 5 or λ = 6) or operating in the low TSR region (λ = 1.5) [23]. For high TSR values, the wind flow is mainly attached to the airfoil, due to the low angles of attack. However, when the TSR is in the low region, the angle of attack of the flow on the airfoil increases, leading to dynamic stall effects that highly influence the turbine performance [23]. Additionally, increasing the turbine solidity value leads to the turbine

operational region becoming narrower and drifting to lower λ values [24]. Thus, high solidity (typically around 0.3–0.5) and low TSR seem favourable for the J-shaped design.

This study aims to develop an optimised J-shaped blade, using a NACA0015 airfoil as reference, to improve the starting torque while sustaining the performance of a Darrieus turbine. The original works on J-shapes [19–21] and more recent studies [25] focused on blades with a hollow and hair-like format, but did not consider the internal geometry of the design. The present work thus evaluates the performance of J-shaped blades with a filled structure. Numerical simulations were performed for six different J-shapes, designed by sectioning the NACA0015 airfoil at various locations and creating cuts with different depths.

2. Numerical Methods

A 2D Computational Fluid Dynamics (CFD) model of an H-Type Darrieus VAWT with NACA0015 airfoil was created and the results were compared to experimental data from the literature. This provided the base model. J-Shapes were then designed and tested numerically. The computational mesh was generated with the commercial ANSYS Integrated Computer Engineering and Manufacturing tool, also known as ICEM-CFD, and the flow solution was obtained with ANSYS Fluent.

2.1. Governing Equations and Turbulence Model

Unsteady Reynolds-Averaged Navier–Stokes (URANS) equations were considered to solve the turbulent flow, where the continuity and momentum equations for incompressible flows can be written as [26]:

$$\frac{\partial \overline{u}_i}{\partial x_i} = 0, \tag{1}$$

$$\rho \frac{\partial \overline{u}_i}{\partial t} + \rho \overline{u}_j \frac{\partial \overline{u}_i}{\partial x_i} = -\frac{1}{\rho}\frac{\partial \overline{P}}{\partial x_i} + \frac{\partial}{\partial x_j}\left(\mu \frac{\partial \overline{u}_i}{\partial x_j}\right) - \frac{\partial \rho \overline{u_i' u_j'}}{\partial x_j}, \tag{2}$$

where $\overline{P}$ and $\overline{u_i}$ are the time-averaged pressure and velocity, respectively, ρ is the density and μ the dynamic viscosity of the fluid, here air. The term $-\rho \overline{u_i' u_j'}$ represents the Reynolds-stress tensor, also denoted τ_{ij}, which depends on the turbulent components of the velocity $\overline{u_i'}$ and $\overline{u_j'}$ [26]. For the URANS approach, τ_{ij} is approximated using a turbulence model, this will be defined below. It should also be noted that the flow incompressibility assumption considered here is fully valid as the Mach number is such that $M < 0.3$.

Previous studies on the numerical modelling of VAWTs considered different approaches, including Spallart–Almaras (SA), k-ϵ based models, Detached Eddy Simulation (DES), and Large Eddy Simulation (LES) [27,28]. The first three above-mentioned models over-estimated the fully turbulent flow in the leading-edge region, leading to inaccuracies in representing the vorticity distribution along the airfoil. LES and DES proved to be more efficient in describing the turbulent phenomenon, but they were also the most demanding in terms of computing resources. Authors in [20,21] and [29] showed that the k-ω SST model was successful in providing good results when compared to experimental data from [30]. Hence, the k-ω SST turbulence model was selected for this work. This model developed by Menter [31] switches automatically from a k-ω definition near the walls to a k-ϵ definition in the bulk flow, which makes this model efficient in the sublayer near the walls, and far away from the walls [32].

$$\frac{D\rho k}{Dt} = \tau_{ij}\frac{\partial u_i}{\partial x_j} - \beta^* \rho \omega k + \frac{\partial}{\partial x_j}\left[(\mu + \sigma_k \mu_t)\frac{\partial k}{\partial x_j}\right], \tag{3}$$

$$\frac{D\rho\omega}{Dt} = \frac{\gamma}{\nu_t}\tau_{ij}\frac{\partial u_i}{\partial x_j} - \beta\rho\omega^2 + \frac{\partial}{\partial x_j}\left[(\mu + \sigma_\omega \mu_t)\frac{\partial \omega}{\partial x_j}\right] + 2\rho(1 - F_1)\frac{\sigma_{\omega_2}}{\omega}\frac{\partial \kappa}{\partial x_j}\frac{\partial \omega}{\partial x_j}, \tag{4}$$

where k is the turbulent kinetic energy, ω the specific turbulence dissipation rate, μ_t the eddy viscosity and F_1 a blending function. The blending function allows the model to behave like the k-ω model near the walls and like the k-ϵ in the outer regions [31]. The other terms, namely β^*, β, σ_κ, σ_ω, $\sigma_{\omega 2}$, and γ, are the model constants [31].

2.2. VAWT Model and Boundary Conditions

The turbine considered was a high-solidity VAWT, as considered experimentally in [30]. A similar set-up was used as in [20,21,29,33,34]. The positions and sizes of the cavity built for the J-shaped airfoil were selected, based on similar studies conducted in [20,35]. The parameters of the model are provided in Table 1. As the central shaft was not included in all previously published studies on the same VAWT, this shaft is not modelled either in the current work.

Table 1. Model parameters.

Parameters	Details
Number of blades	3
Rated power	3.5 kW
Chord length	0.4 m
Turbine radius	1.25 m
Solidity	0.48
Mounting point	0.2 m
Rund-off at the trailing edge	0.004 m
Normal operating conditions	$6 < V_{wind}$ (m/s) < 16

The computational domain is shown in Figure 1 [36,37], where D is the diameter of rotation of the blades, and d_c is the external diameter of the rotating region, which is 1.2 times the turbine diameter.

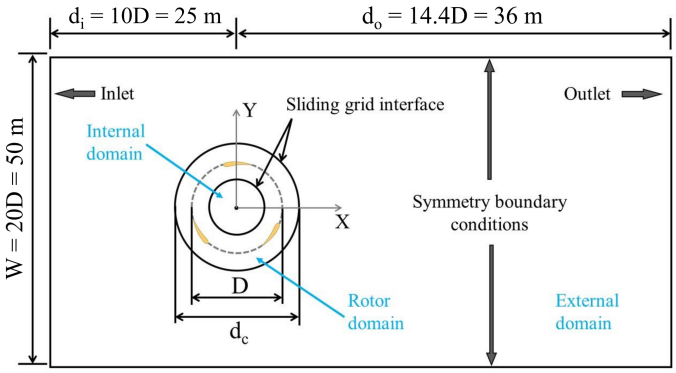

Figure 1. Computational domain regions (blue colour) and boundary conditions (black colour).

Velocity inlet and pressure outlet boundary conditions were considered for the inlet and outlet of the computational domain, and the top and bottom boundaries were set as symmetry, see Figure 1. Air at 10 m/s was injected into the system for all simulations, with turbulent intensity and turbulent viscosity ratio settings of 5% and 10, respectively. Note that these turbulence values are default values in the software. They remained unchanged in all simulations, as they provided good results during the model validation phase, see Section 3.3.

2.3. Mesh Generation

A structured mesh was generated with ICEM CFD and refined near the rotating turbine to reach a non-dimensional distance at the wall y^+ less than 1, which is in agreement with the requirements of the k-ω SST turbulence model. Figure 2 shows the final meshed domain for the VAWT with NACA0015 airfoil, including a closer view of the rotating region.

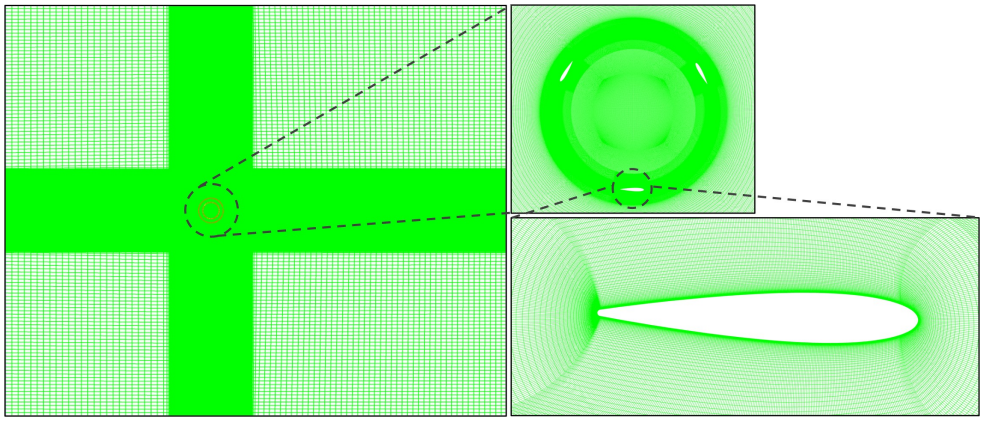

Figure 2. Details of the computational mesh.

2.4. Solver Description

The time step of the transient simulation was based on azimuthal increments. Four different rotational speeds ω (rad/s) were considered to simulate the four λ of interest, ranging from 0.2 (to study the starting torque), 1.25, 1.6, and 2. The calculation of ω was performed through Equation (5).

$$\lambda = \frac{\omega R}{V} \rightarrow \omega = \frac{\lambda V}{R}, \tag{5}$$

where R is the turbine radius (m) and V the wind velocity (m/s).

The azimuthal increment at each time step was set at 0.5°, following a similar numerical work reported in [29]. Based on the values of ω and the azimuthal increment, the corresponding time steps were calculated through Equation (6). The details of both calculated variables are summarised in Table 2.

$$Time\ step\ size\ (s) = 2\pi \frac{azimuthal\ increment}{360} \frac{1}{\omega}. \tag{6}$$

Table 2. Angular velocity and time-step used for different λ.

(λ)	ω (rad/s)	Time Step (s)
0.20	1.6	5.454×10^{-3}
1.25	10	8.727×10^{-4}
1.60	12.8	6.817×10^{-4}
2.00	16	5.454×10^{-4}

The Semi-Implicit Method for Pressure Linked Equations (SIMPLE) algorithm was selected for the pressure-velocity coupling, with a second-order upwind method for the momentum, turbulent kinetic energy, and specific dissipation rate. A maximum number of 100 iterations per time step was applied, providing residuals lower than 10^{-5} for each time step.

The power coefficient (C_P) and torque coefficient (C_m) were considered to assess the performance of the wind turbines investigated here. C_P is the ratio between the electric power and the actual power available on the wind and is a measure of the efficiency of the wind turbine, which is a non-linear function of tip speed ratio and pitch angle.

$$C_P = \frac{P}{\frac{1}{2}\rho A V^3}, \tag{7}$$

where P is the electric output power (W). The denominator in Equation (7) indicates the input power of the wind, where ρ is the density of air (kg/m^3), A is the turbine swept area,

i.e., its diameter multiplied by its height (m^2) and V is the wind speed (m/s). The torque coefficient is calculated as:

$$C_m = \frac{T}{\frac{1}{2}\rho A R V^2}, \quad (8)$$

with T the torque produced by the turbine (N·m). The correlation between C_P and C_m is shown through Equation (9).

$$C_P = C_m \frac{\omega R}{V} = C_m \lambda. \quad (9)$$

3. Results and Discussion

The main outcomes of the research are described in the following sections. A mesh independence study was conducted, and the number of revolutions required for each simulation was determined. The VAWT model results are then compared against experimental data from the literature. Finally, design improvements and solutions to J-shaped blades are provided.

3.1. Mesh Independence Study

To ensure that CFD results do not depend on the mesh density, four meshes were assessed numerically, comprising between 100,000 and 1 million cells. The C_P values were extracted at the point of maximum efficiency reported for the turbine, i.e., λ = 1.6, and compared with the reference C_P value from Daróczy et al. [29]. Table 3 summarises the C_P values obtained with all meshes considered for the 2D VAWT model with NACA0015 airfoils. As can be noticed, a convergence of the C_P value is reached with a mesh of 785,963 cells, and increasing the number of cells does not change the value. However, it should also be mentioned that the difference between Mesh 3 (785,963 cells) and Mesh 2 (462,678 cells) is less than 2.2%. To reduce computational costs, Mesh 2 was, therefore, considered for the rest of the CFD work.

Table 3. Results of the mesh independence study.

Mesh	Total Number of Cells	Number of Cells in Rotor Region	Number of Cells in Internal Region	C_P
1	100,228	66,621	11,495	0.3963
2	462,678	305,721	51,405	0.4061
3	785,963	518,516	92,220	0.4151
4	1,043,238	714,351	98,505	0.4153

Results reported in Table 3 are shown in Figure 3, and they are compared with numerical results from Daróczy et al. [29]. The percentage of error between the current C_P results obtained with Mesh 2 and the Daróczy et al. [29] results is around 1.7%. This confirms that Mesh 2 can be safely used at a lower computational cost than Mesh 3.

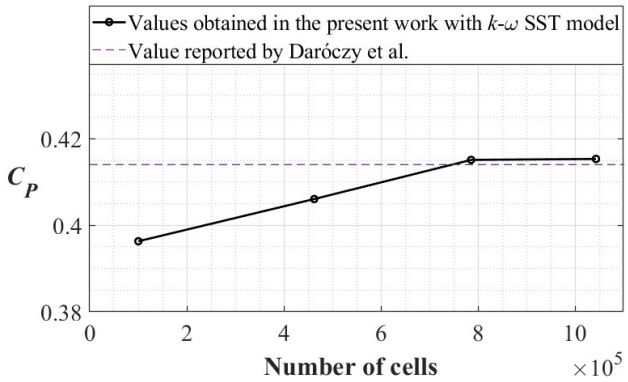

Figure 3. CFD-based C_P vs. results from Daróczy et al. [29].

Zamani et al. [20] carried out a mesh independence study for both NACA0015 and J-shaped airfoils. They concluded that similar mesh sizes provided mesh-independent results for both airfoils. The mesh independence study was thus not repeated for all J-shaped airfoils considered in the present work. The strategy was to perform it once for the reference airfoil and consider the meshing strategy and mesh size suitable for all modified J-shaped airfoils.

3.2. Number of Revolutions

The effects due to the number of blade revolutions was studied for the VAWT, and the outcome is presented in Figure 4. It appears clearly that simulations with the highest λ need more revolutions to reach the convergence of the C_P value, while low values of λ need fewer revolutions. This agrees with conclusions from the literature, e.g., [36]. Based on Figure 4 and to reduce computational time, 5 revolutions were considered at low λ (0.2 and 1.25) and 15 revolutions were applied at high λ (1.6 and 2.0).

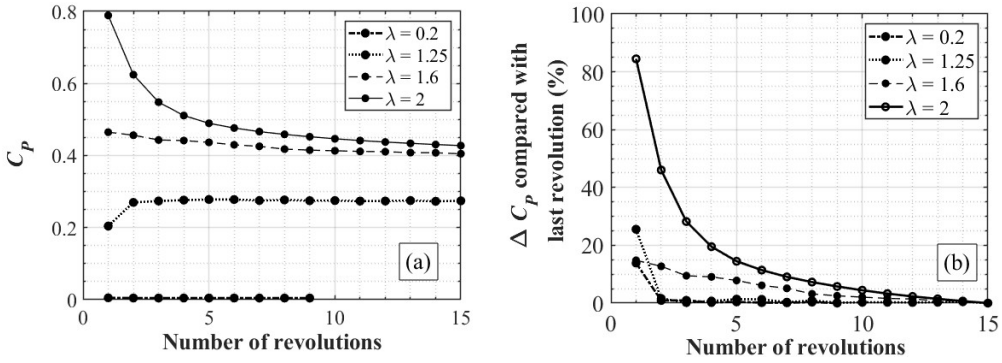

Figure 4. Convergence of the simulated C_P values, based on the number of revolutions at various λ (**a**) and C_P % error based on the number of revolutions (**b**).

3.3. VAWT Model Validation

CFD-based C_P results obtained for the VAWT were compared with results extracted from the literature, see Figure 5, with experimental results from Bravo et al. [30], and numerical work from Daróczy et al. [29].

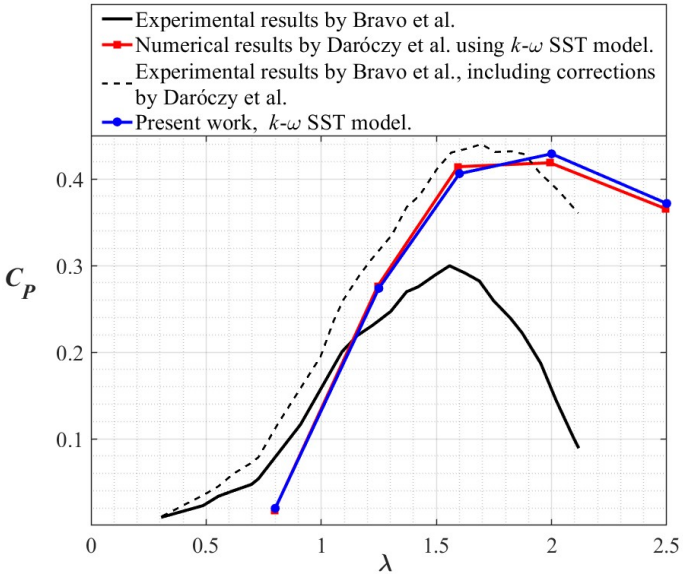

Figure 5. C_P comparison between the present study, the experimental results from Bravo et al. [30], and the numerical work from Daróczy et al. [29].

A good match is obtained between simulated results obtained here and those from Daróczy et al. [29]. However, both numerical results differ significantly from the experimental data, especially regarding the maximum C_P and the shape of the curve after the maximum value is achieved. Daróczy et al. [29] studied this phenomenon and found out that by considering the shaft mechanical losses due to friction and by adding a cubic correction to account for the struts' aerodynamic losses, numerical and experimental results had a better agreement. Mechanical losses were obtained experimentally in [38] and the cubic correction was estimated by the authors to fit the numerical results ($\Delta C_P = 0.02\lambda^3$). The resulting corrected experimental curve is also shown in Figure 5. It is worth noting that 3D effects can have an impact on those results as all numerical simulations presented in Figure 5 were conducted in 2D. Results obtained with 2D simulations are known to generally over-predict results.

The flow inside the turbine was analysed. Different parameters including velocity, pressure, and turbulence characteristics were evaluated with the flow solver. As an example, Figure 6 shows the flow velocity contours around the turbine at different λ.

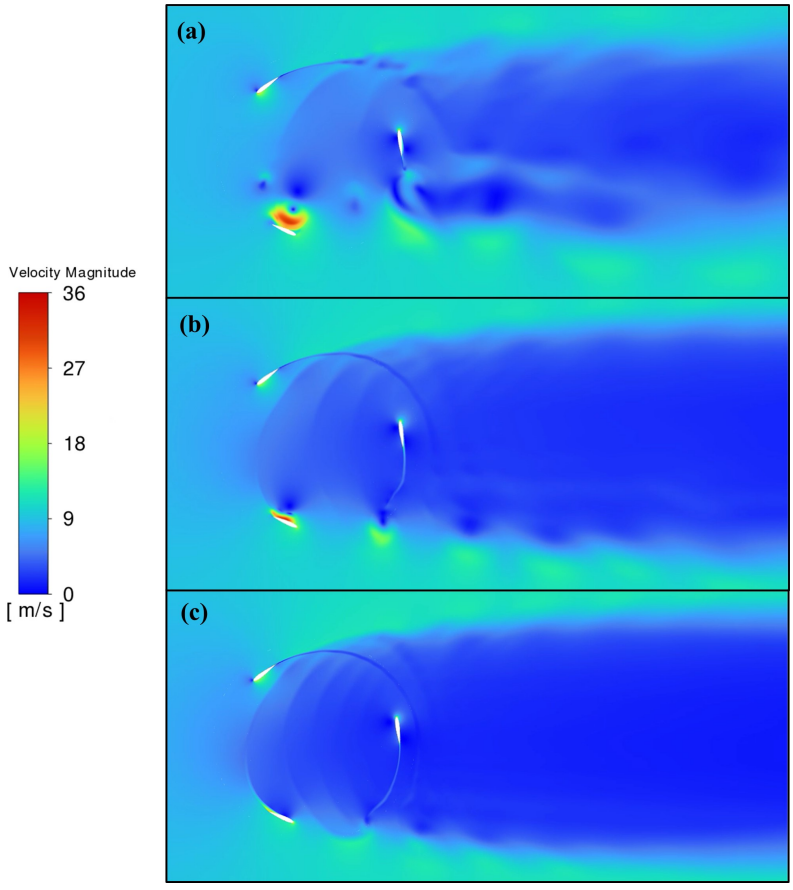

Figure 6. Velocity contours for the VAWT with NACA0015 airfoil at different λ: (**a**) $\lambda = 1.25$; (**b**) $\lambda = 1.6$; (**c**) $\lambda = 2$.

The dynamic stall phenomenon is present in the region of low λ, see Figure 6a for $\lambda = 1.25$ and Figure 6b for $\lambda = 1.6$. As λ increases, the flow in the upwind region reaches the airfoil with lower angles of attack, and separation effects are reduced, see Figure 6c. The dynamic stall effect is responsible for the performance of the turbine in the maximum efficiency region, for $\lambda = 1.6$. This effect increases the torque produced in the upwind region, for azimuthal angles between 50° and 140°, where the dynamic stall effect is predominant. It leads to a torque decay in the leeward region, between around 150° and 210°, where the formed vortices separate and produce negative torques on the airfoil,

before travelling downstream, as seen in Figure 6b. This process is illustrated in Figure 7, showing the torque produced by one airfoil in one rotation.

Numerical results were compared with those from Zamani et al. [21] in Figure 7. A good match was obtained, the main differences being in the lower values of the peak torque and the torque produced downwind. The reason for that difference is most certainly due to the fact Zamani et al.'s CFD results were obtained with a 3D model, where more losses are expected than with a 2D model.

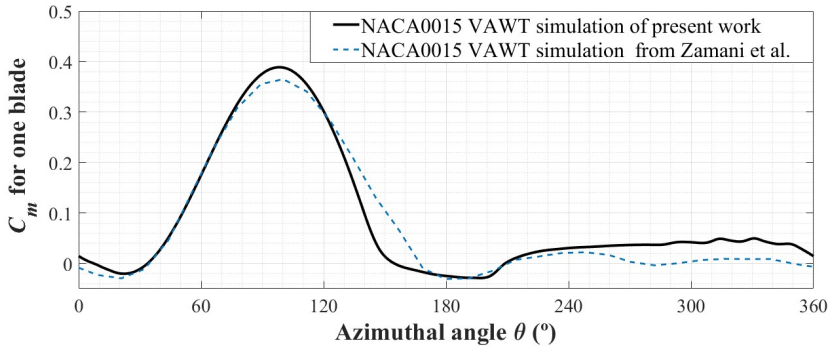

Figure 7. Variation of the torque coefficient of one airfoil with the azimuthal angle at λ = 1.6 in the present work and comparison with the results obtained by Zamani et al. [21].

3.4. Design Improvement

Six J-shaped design improvements were proposed, with inner and outer cuts applied on a NACA0015 airfoil, see Table 4. CFD simulations were performed for all six designs for TSR values studied previously, i.e., for λ = 1.25, 1.6, and 2.0, to evaluate the designs under normal operational conditions, and for λ = 0.2 to study the starting torque. As cutting part of the internal geometry introduces new areas in which the flow needs to be resolved, the mesh had to be checked and refined where necessary next to the airfoil, to ensure that a y^+ value less than 1 was still obtained and that the requirements of the k-ω SST turbulence model were still fulfilled.

One typical example of the meshing strategy used for a proposed design, in this case for the J1 airfoil, is shown in Figure 8.

Table 4. J-shaped designs.

Description of the Designs	Design Illustration
J1: The airfoil is created such that the cavity on the top starts at around 40% of the reference airfoil chord length. The pressure side of the airfoil is designed to be a bit more horizontal (0.023 m) than the curved pressure side of the reference airfoil. The second picture illustrates the comparison between the J1 design and the original NACA0015 airfoil.	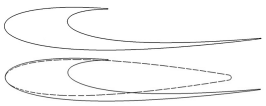
J2: The airfoil is a mirrored version of the J1 shape. The objectives were (1) to have a clear performance comparison between the inner and outer cavity placements, and (2) to understand how the formed vortices behave inside the cavity, along with the impact on the turbine's performance after dynamic stall.	
J3: The opening starts at the location of maximum thickness (30% of the chord length) and with a 90° step of 1/8th of the thickness. The internal curvature is equal to the lower edge of the reference airfoil. The trailing edge was rounded off (2 mm). The objective was to establish how performance is affected when a cavity is present on the pressure side of the airfoil.	

Table 4. *Cont.*

Description of the Designs	Design Illustration
J4: This model was prepared by offsetting the reference airfoil. The airfoil was sectioned at half the maximum thickness from the leading edge. The reason was to improve the performance and to assess the effects of a larger size cavity.	
J5: A straight tapered cut was made on the reference airfoil, starting from the highest thickness point to the trailing edge. The objective was to increase the lift-to-drag ratio by introducing a straight cut on the pressure side, following the idea by [35]. The trailing edge was rounded off (2 mm).	
J6: This shape is a flipped version of the J5 shape.	

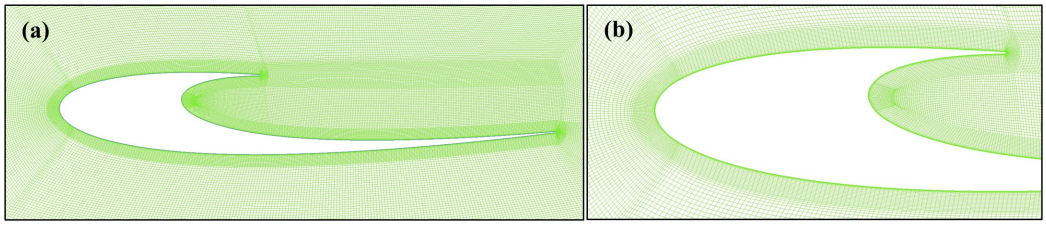

Figure 8. Structured mesh around the J1 airfoil. (**a**) Complete airfoil and (**b**) Detail of the near wall region at the leading edge.

Standard Operational Conditions

Figure 9 shows the CFD-based torque coefficient values, with the cut in the external face, i.e., for the J1, J4, and J6 models, under standard operational conditions (λ of 1.25–2.0). Figure 10 shows the same results for the airfoils with the cut, this time, in the internal face (J2, J3, and J5 models).

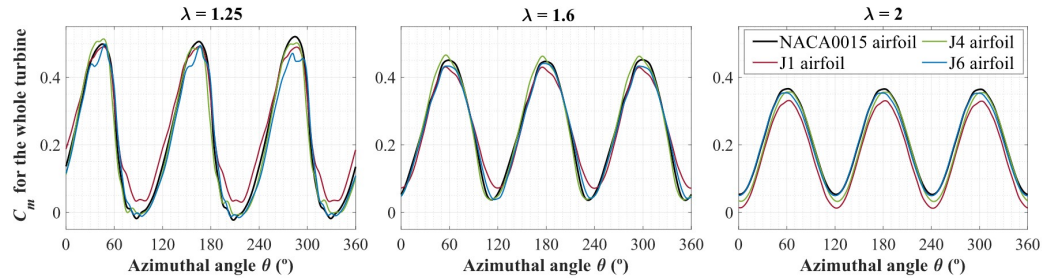

Figure 9. C_m value for external face J-shaped designs.

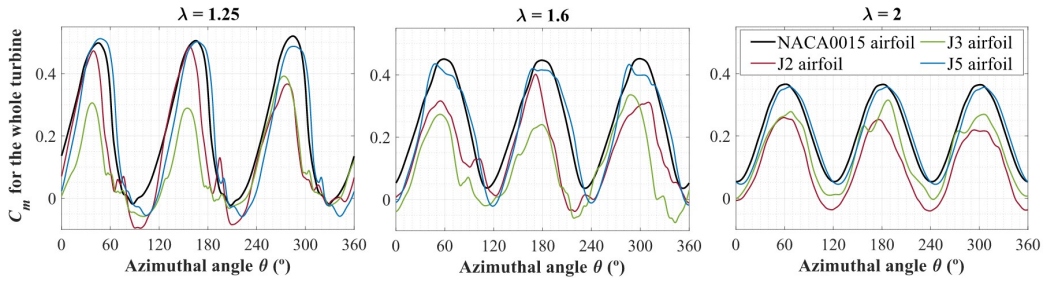

Figure 10. C_m value for internal face J-shaped designs.

As can be seen, airfoils with an external cut systematically provide better results, in terms of torque produced, compared to the airfoils with an internal cut. All the formers show similar torques compared to the NACA0015 airfoil. In addition, the torque produced by the airfoils with external cut, is more stable in time compared to the torque from the airfoils with an internal cut. This can be explained by the unpredictability of the high flow separation taking place for the airfoils with an internal cut.

The J1 airfoil showed a better performance than the NACA0015 airfoil in most of the operational region. For λ of 1.25 and 1.6, the J1 airfoil produced the same torque as the NACA0015 airfoil, but was more uniform, thus introducing advantages in terms of fatigue stresses and power production. However, for a λ of 2, the J1 airfoil performance started to be lower than for the NACA0015 airfoil.

To better understand the flow behaviour around the different airfoils, the pathlines were analysed at several azimuthal angles. Figure 11 shows examples of the results for four airfoils at two positions, namely the initial part of the upwind region, and the leeward region, for the TSR of maximum efficiency (λ = 1.6).

When looking at the pathlines in the upwind region in Figure 11, it appears that vortexes formed inside the cavity of the J-shaped airfoil. The number and the shape of those vortexes depend on the size and position of the cavity. One first conclusion regarding this aspect is that for cuts placed on the internal face of the airfoil, the vortex forms in the suction side when the blades pass through the upwind, increasing the drag. This can be seen with the J3 airfoil in Figure 11c, where the high velocities of the vortex near the wall translate into low pressures on the trailing edge.

However, the airfoil with the cut in the external face shows vortexes on the pressure side; such a cut does not have a large impact on the flow conditions. Only a small decrease in the torque is produced in that region, as seen in Figure 9, due to the small increase in drag.

Regarding the pathlines in the leeward region, almost all airfoils present important flow separation, similarly to the NACA0015 described previously in Section 3.3. The largest vortex appears when the cuts are in the internal face (c.f. J3 airfoil in Figure 11c). This translates into a decrease in the lowest peak of torque in Figure 10, even becoming negative.

It is worth noting that the airfoil with the lowest vortex formation is the J1 design, as seen in Figure 11b. This agrees with the results displayed previously in Figure 9, where the lowest torque value for that airfoil produced in the leeward region, was higher than for the rest of the airfoil. Based on that outcome, the flow around the turbine with the J1 airfoil was investigated in detail. Figure 12 thus illustrates examples of the velocity and turbulence fields for this airfoil, again for λ = 1.6.

Two main differences can be seen in the velocity contours between the turbine with NACA0015 airfoils and the one with J1 airfoils in Figure 12 (left). The wake left by the airfoil in the downwind region is more unstable for the J1 airfoil. As seen previously in Figure 10, the cut in the suction side makes the flow around the airfoil more unstable, producing those oscillations in the wake of the J1 airfoil case. The second important effect seen in the velocity field is the vortex shedding in the leeward region. As could be seen in the pathlines in Figure 11, the J1 airfoil significantly reduces the vortex formation and shedding when passing through the leeward zone.

To analyse the impact of this vortex formation in more detail, the turbulence intensity contour plots are shown in Figure 12 (right). In line with the previous discussions, the turbulence intensity in the leeward region is more important for the NACA0015 airfoil due to the vortex formation and shedding.

Another interesting point can be highlighted from the turbulence intensity contour plots in Figure 12 (right). As explained previously, higher turbulence is present in the wake of the airfoil in the downwind region for the J1 airfoil case compared to the NACA0015 airfoil, but lower turbulence is produced in the leeward region. The combination of both effects thus produces a wake behind the turbine that is more uniform for the J1 airfoil.

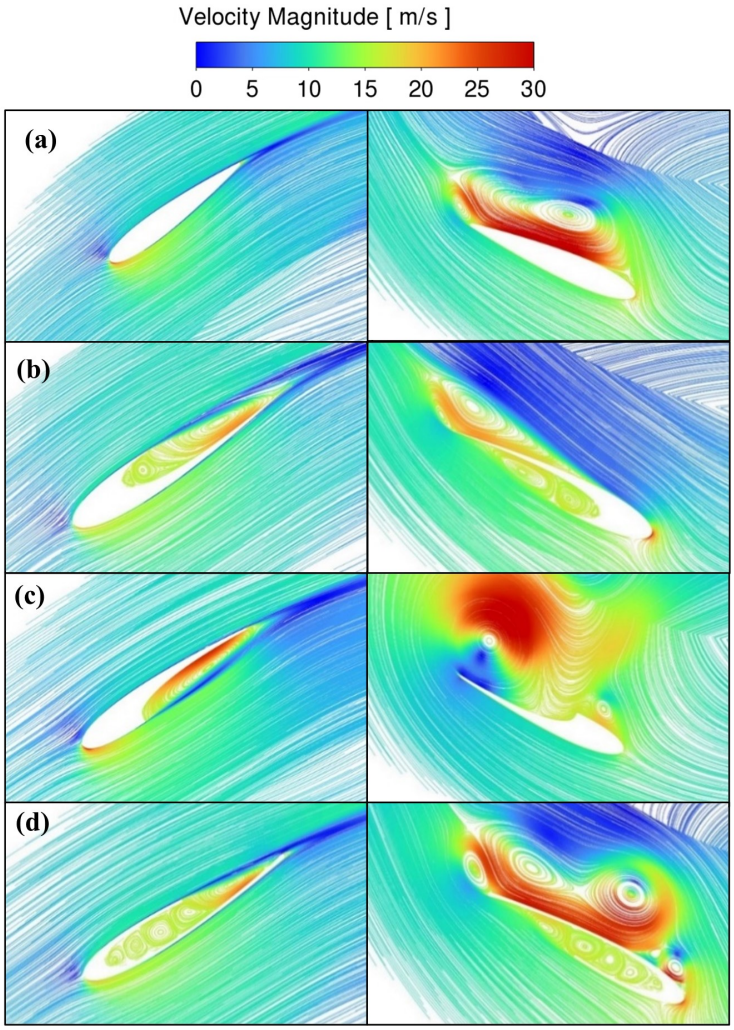

Figure 11. Pathlines of the flow relative to the airfoil in the upwind region (left) and in the leeward region (right) at λ =1.6 and for 4 different airfoils: (**a**) NACA0015, (**b**) J1, (**c**) J3, (**d**) J4.

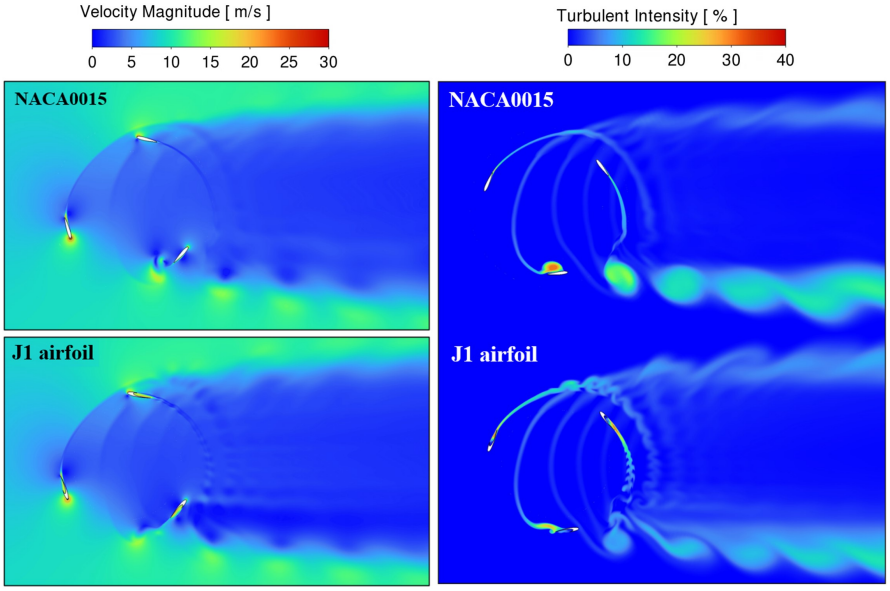

Figure 12. Velocity magnitude (**left**) and turbulence intensity (**right**) contour plots around the VAWT for the cases with NACA0015 airfoils and with J1 airfoils at λ = 1.6.

Starting Torque

The proposed airfoils were assessed in normal operational conditions in the previous section. The starting torque is now investigated. As mentioned previously, the starting torque was tested by considering the VAWT at a very low TSR, λ = 0.2. This value is low enough to provide a flow field similar to the undisturbed one, but high enough to enable transient simulations with small time steps, in the order of 10^{-3} s, as considered for the other λ values tested. Having a flow field similar to the undisturbed one means that air approaches the airfoil with similar direction as the freestream wind, replicating starting conditions. The mean torque was obtained for all cases under such conditions, see Figure 13.

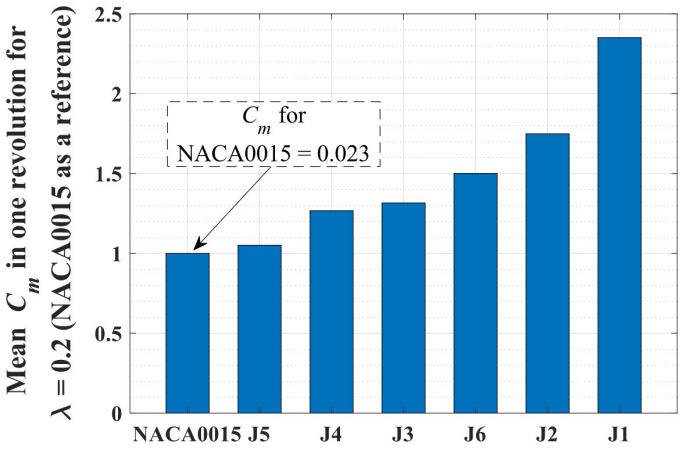

Figure 13. Comparison of the VAWT starting torque between the NACA0015 airfoil and the J-shapes proposed. Results presented relative to the torque coefficient for the NACA0015 airfoil.

Figure 13 shows the relative mean torque for each case, compared to those obtained for the NACA0015 airfoil. As can be seen, all six simulated airfoils display a higher starting torque compared to the NACA0015 airfoil, with a wide range of variation, going from a 5% improvement for the J5 airfoil to a 135% improvement for the J1 airfoil. The main reason for such starting torque improvements is that all the cuts of the airfoil introduce extra drag when the airfoil passes through the leeward region. To evaluate this effect, the pathlines for one airfoil, J1, were analysed.

Figure 14 illustrates how the J-shape improves the torque produced in the leeward region for very low λ. The pathlines display how a vortex is formed inside the airfoil, leading to a momentum change in the external flow by modifying its direction, producing a drag boost. The static pressure in the suction side of the airfoil for the case of the J1 airfoil also creates a resultant force, whose tangential component is increased due to the 'cup' shape, therefore acting like a Savonius turbine. These two related effects lead to an improvement of the starting torque in comparison with the symmetrical NACA0015 airfoil, following hypotheses and results from the literature [19,20].

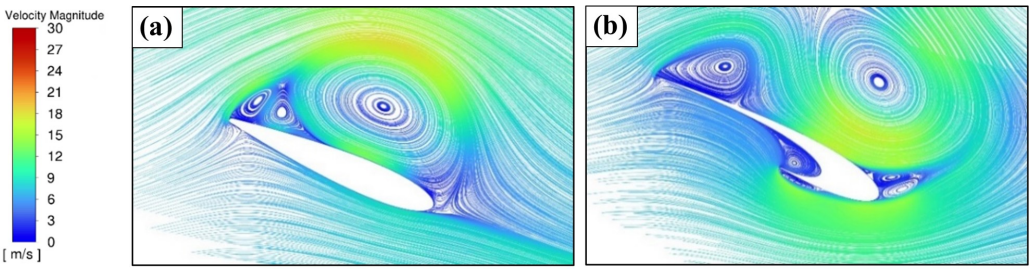

Figure 14. Pathlines of the flow relative to the airfoil at the leeward region at λ = 0.2 and for two different airfoils: (**a**) NACA0015, (**b**) J1.

This improvement however depends on the design considered. The most promising results were established with the J1 and J2 airfoils. These two designs share the same cut of the airfoil but at different locations, external for J1 and internal for J2. Another interesting option when evaluating the normal operational conditions was the J4 airfoil. However, the depth of the cut reduced the starting torque improvement in comparison with J1 and J2 airfoils, as summarised previously in Figure 13.

4. Conclusions

This study investigated six different J-shaped blade designs for VAWT. The designs followed the original idea of J-shaped airfoil proposed in [19,20], however presenting a filled structure rather than a hair-like shape. A 3 kW Darrieus turbine with NACA0015 blades, tested experimentally by Bravo et al. [30], was replicated to validate the numerical model, and different cut geometries were introduced on the blades to evaluate their effect on the turbine performance. Conclusions can be drawn from the numerical investigation:

- The blades with a cut in the external face systematically performed better than the ones with an internal cut. The latter presented an unstable behaviour due to important vortices formation.
- The proposed J1 airfoil provided the best performance in normal operating conditions of the turbine, producing the same power at the maximum efficiency point compared to the NACA0015 case, but more uniform, thus introducing advantages in terms of fatigue stresses.
- The starting torque of the turbine was improved with all the cut geometries tested compared to the NACA0015 airfoil base case. The highest improvement was obtained for the J1 airfoil, which provided a starting torque 135% higher than for the NACA0015 airfoil.

Future studies will cover effects such as blade tip vortices and a more complete description of the turbulence phenomena; this will be achieved with a 3D model. Additionally, vibrations caused by vortex shedding and their effects on the blades' strength could be investigated.

Author Contributions: Conceptualization, A.G.A., R.E.S., H.M., S.S.R. and D.C.; methodology, A.G.A., R.E.S., H.M., S.S.R. and D.C.; investigation, A.G.A., R.E.S., H.M., S.S.R. and D.C.; writing—original draft preparation, A.G.A., R.E.S., H.M., S.S.R., D.C. and P.G.V.; writing—review and editing, A.G.A., R.E.S., H.M., S.S.R., D.C. and P.G.V.; supervision, P.G.V. All authors have read and agreed to the published version of the manuscript.

Funding: This research received no external funding.

Institutional Review Board Statement: Not applicable.

Informed Consent Statement: Not applicable.

Data Availability Statement: Not applicable.

Conflicts of Interest: The authors declare no conflict of interest.

References

1. Parakkal, J.U.; El Kadi, K.; El-Sinawi, A.; Elagroudy, S.; Janajreh, I. Numerical analysis of VAWT wind turbines: Joukowski vs classical NACA rotor's blades. *Energy Procedia* **2019**, *158*, 1194–1201. [CrossRef]
2. Hau, E. *Wind Turbines: Fundamentals, Technologies, Application, Economics*; Springer Science & Business Media: Berlin/Heidelberg, Germany, 2013.
3. Amet, E.; Maître, T.; Pellone, C.; Achard, J.L. 2D numerical simulations of blade-vortex interaction in a Darrieus turbine. *J. Fluids Eng.* **2009**, *131*, 111103. [CrossRef]
4. Agha, A.; Chaudhry, H.; Wang, F. Diffuser Augmented Wind Turbine (DAWT) Technologies: A Review. *Int. J. Renew. Energy Res.* **2018**, *8*, 1369–1385.
5. Nunes, M.; Junior, A.; Oliveira, T. Systematic review of diffuser-augmented horizontal-axis turbines. *Renew. Sustain. Energy Rev.* **2020**, *133*, 110075. [CrossRef]

6. Jafari, S.; Kosasih, B. Flow analysis of shrouded small wind turbine with a simple frustum diffuser with computational fluid dynamics simulations. *J. Wind Eng. Ind. Aerodyn.* **2014**, *125*, 102–110. [CrossRef]
7. Ohya, Y.; Karasudani, T. A Shrouded Wind Turbine Generating High Output Power with Wind-lens Technology. *Energies* **2010**, *3*, 634–649. [CrossRef]
8. García Auyanet, A.; Verdin, P. Numerical Study of the Effect of Flap Geometry in a Multi-Slot Ducted Wind Turbine. *Sustainability* **2022**, *14*, 12032. [CrossRef]
9. Migliore, P. Comparison of NACA 6-series and 4-digit airfoils for Darrieus wind turbines. *J. Energy* **1983**, *7*, 291–292. [CrossRef]
10. Kadlec, E.G. *Characteristics of Future Vertical-Axis Wind Turbines*; Technical Report SAND-79-1068; Sandia National Labs.: Albuquerque, NM, USA, 1978.
11. Klimas, P.C. *Airfoil Treatments for Vertical Axis Wind Turbines;* Sandia National Labs.: Albuquerque, NM, USA, 1985.
12. Maruyama, Y.; Shimura, M.; Yoshie, R.; WEI, R.; SEKI, K. Development of vertical axis wind turbine with straight blades suitable for buildings. *JWE* **2001**, *89*, 265–268.
13. Claessens, M. The Design and Testing of Airfoils for Application in Small Vertical Axis Wind Turbines. Master's Thesis, Delft University of Technology, Delft, The Netherlands, 2006.
14. Gupta, R.; Biswas, A.; Sharma, K. Comparative study of a three-bucket Savonius rotor with a combined three-bucket Savonius–three-bladed Darrieus rotor. *Renew. Energy* **2008**, *33*, 1974–1981. [CrossRef]
15. Mohan Kumar, P.; Sivalingam, K.; Lim, T.C.; Ramakrishna, S.; Wei, H. Strategies for enhancing the low wind speed performance of H-Darrieus wind turbine-Part 1. *Clean Technol.* **2019**, *1*, 185–204. [CrossRef]
16. Wong, K.; Chong, W.; Sukiman, N.; Poh, S.; Shiah, Y.; Wang, C. Performance enhancements on vertical axis wind turbines using flow augmentation systems: A review. *Renew. Sustain. Energy Rev.* **2017**, *73*, 904–921. [CrossRef]
17. Mohamed, O.S.; Ibrahim, A.A.; Etman, A.K.; Abdelfatah, A.A.; Elbaz, A.M. Numerical investigation of Darrieus wind turbine with slotted airfoil blades. *Energy Convers. Manag. X* **2020**, *5*, 100026. [CrossRef]
18. Abdolahifar, A.; Karimian, S. A comprehensive three-dimensional study on Darrieus vertical axis wind turbine with slotted blade to reduce flow separation. *Energy* **2022**, *248*, 123632. [CrossRef]
19. Chen, J.; Yang, H.; Yang, M.; Xu, H. The effect of the opening ratio and location on the performance of a novel vertical axis Darrieus turbine. *Energy* **2015**, *89*, 819–834. [CrossRef]
20. Zamani, M.; Maghrebi, M.J.; Varedi, S.R. Starting torque improvement using J-shaped straight-bladed Darrieus vertical axis wind turbine by means of numerical simulation. *Renew. Energy* **2016**, *95*, 109–126. [CrossRef]
21. Zamani, M.; Nazari, S.; Moshizi, S.A.; Maghrebi, M.J. Three dimensional simulation of J-shaped Darrieus vertical axis wind turbine. *Energy* **2016**, *116*, 1243–1255. [CrossRef]
22. Mohamed, M. Criticism study of J-Shaped Darrieus wind turbine: Performance evaluation and noise generation assessment. *Energy* **2019**, *177*, 367–385. [CrossRef]
23. Rezaeiha, A.; Montazeri, H.; Blocken, B. Towards optimal aerodynamic design of vertical axis wind turbines: Impact of solidity and number of blades. *Energy* **2018**, *165*, 1129–1148. [CrossRef]
24. Brusca, S.; Lanzafame, R.; Messina, M. Design of a vertical-axis wind turbine: How the aspect ratio affects the turbine's performance. *Int. J. Energy Environ. Eng.* **2014**, *5*, 333–340. [CrossRef]
25. Pan, L.; Zhu, Z.; Xiao, H.; Wang, L. Numerical Analysis and Parameter Optimization of J-Shaped Blade on Offshore Vertical Axis Wind Turbine. *Energies* **2021**, *14*, 6426. [CrossRef]
26. Wilcox, D. *Turbulence Modeling for CFD*, 3rd ed.; DCW Industries: La Cañada, CA, USA, 2006.
27. Ferreira, C.S.; Bijl, H.; Van Bussel, G.; Van Kuik, G. Simulating dynamic stall in a 2D VAWT: Modeling strategy, verification and validation with particle image velocimetry data. *Proc. J. Phys. Conf. Ser.* **2007**, *75*, 012023. [CrossRef]
28. Simao Ferreira, C.; Van Bussel, G.; Van Kuik, G. 2D CFD simulation of dynamic stall on a vertical axis wind turbine: Verification and validation with PIV measurements. In Proceedings of the 45th AIAA Aerospace Sciences Meeting and Exhibit, Reno, NV, USA, 8–11 January 2007; p. 1367.
29. Daróczy, L.; Janiga, G.; Petrasch, K.; Webner, M.; Thévenin, D. Comparative analysis of turbulence models for the aerodynamic simulation of H-Darrieus rotors. *Energy* **2015**, *90*, 680–690. [CrossRef]
30. Bravo, R.; Tullis, S.; Ziada, S. Performance testing of a small vertical-axis wind turbine. In Proceedings of the 21st Canadian Congress of Applied Mechanics, Toronto, ON, Canada, 3–7 June 2007; pp. 3–7.
31. Menter, F.R. Two-equation eddy-viscosity turbulence models for engineering applications. *AIAA J.* **1994**, *32*, 1598–1605. [CrossRef]
32. Loyseau, X.; Verdin, P.; Brown, L. Scale-up and turbulence modelling in pipes. *J. Pet. Sci. Eng.* **2018**, *162*, 1–11. [CrossRef]
33. Lanzafame, R.; Mauro, S.; Messina, M. 2D CFD modeling of H-Darrieus wind turbines using a transition turbulence model. *Energy Procedia* **2014**, *45*, 131–140. [CrossRef]
34. McLaren, K.; Tullis, S.; Ziada, S. Computational fluid dynamics simulation of the aerodynamics of a high solidity, small-scale vertical axis wind turbine. *Wind Energy* **2012**, *15*, 349–361. [CrossRef]
35. Zhang, T.t.; Huang, W.; Wang, Z.g.; Yan, L. A study of airfoil parameterization, modeling, and optimization based on the computational fluid dynamics method. *J. Zhejiang Univ. Sci. A* **2016**, *17*, 632–645. [CrossRef]
36. Rezaeiha, A.; Montazeri, H.; Blocken, B. Towards accurate CFD simulations of vertical axis wind turbines at different tip speed ratios and solidities: Guidelines for azimuthal increment, domain size and convergence. *Energy Convers. Manag.* **2018**, *156*, 301–316. [CrossRef]

37. Rezaeiha, A.; Kalkman, I.; Blocken, B. CFD simulation of a vertical axis wind turbine operating at a moderate tip speed ratio: Guidelines for minimum domain size and azimuthal increment. *Renew. Energy* **2017**, *107*, 373–385. [CrossRef]
38. Fiedler, A.J.; Tullis, S. Blade offset and pitch effects on a high solidity vertical axis wind turbine. *Wind. Eng.* **2009**, *33*, 237–246. [CrossRef]

https://dspace.org/

CFD-based j-shaped blade design improvement for vertical axis wind turbines

García Auyanet, Antonio; Santoso, Rangga E.; Mohan, Hrishikesh; Rathore, Sanvay S.; Chakraborty, Debapriya ...

2022-11-15
MDPI
https://doi.org/10.3390/su142215343
Auyanet AG, Santoso RE, Mohan H, et al., (2022) CFD-based j-shaped blade design improvement for vertical axis wind turbines. Sustainability, Volume 14, Issue 22, November, Article number 15343

Downloaded from a DSpace repository. https://dspace.org/